



Rupture imaging of the 2021 Ms 6.4 Yangbi, China, earthquake: Implications for the diffuse deformation in the northern region of the Red River fault

Shiming Liang^a, Rumeng Guo^{b,*}, Hongfeng Yang^{c,d,*}, Xiongwei Tang^{b,e}, Xiaoxue Xu^f, Weijun Gan^a

^a State Key Laboratory of Earthquake Dynamics, Institute of Geology, China Earthquake Administration, Beijing, China

^b State Key Laboratory of Geodesy and Earth's Dynamic, Innovation Academy for Precision Measurement Science and Technology, Chinese Academy of Sciences, Wuhan, China

^c Earth System Science Programme, The Chinese University of Hong Kong, Shatin, Hong Kong, China

^d Shenzhen Research Institute, The Chinese University of Hong Kong, Shenzhen, Guangdong, China

^e College of Earth and Planetary Sciences, University of Chinese Academy of Sciences, Beijing, China

^f The Second Monitoring and Application Center, China Earthquake Administration, Xi'an, China

ARTICLE INFO

Keywords:

Yangbi earthquake
Kinematic rupture process
Fault immaturity
Rupture cascade
Diffuse strain partitioning

ABSTRACT

In May 2021, a Ms 6.4 earthquake occurred in the Yangbi Country, Yunnan, China, located in the northern region of the Red River fault, resulting in three deaths. It is a typical foreshock-mainshock-aftershock sequence. However, the kinematic rupture process and the interplay between foreshocks, the mainshock, and aftershocks associated with the Yangbi event remain controversial. Here, we decipher the detailed rupture process associated with this moderate event by jointly inverting the teleseismic body waves, three-component regional waveform, near-field Global Positioning System offsets, and Interferometric Synthetic Aperture Radar data. Results show that the rupture expands as a narrow slip-pulse that propagates southeastward. This event is dominated by the dextral movements with minor normal components, cohere with the tectonic shear and dilation strain partitioning. The high slip is concentrated within the depth range of 5–13 km, spanning ~12 km along strike. A significant shallow slip deficit is identified, perhaps related to the fault being immature. The foreshocks, coseismic slips, and aftershocks reveal a complementary pattern, together releasing the accumulated stresses on the fault. Their distribution areas and Coulomb stress changes suggest that the Yangbi seismic sequence follows the rupture cascade. The absence of large earthquakes, dispersed seismicity, and diffuse strain rate patterns indicate that strain accumulates over a wide area around the northern region of the Red River fault, leading to small-scale ruptures distributed over the area and a low possibility of $M \geq 6.5$ events in the near future.

1. Introduction

1.1. Tectonic settings of the Red River fault

The continuous collision between the Indian and Eurasian plates in the past ~50 Ma results in the rapid uplift of the Tibetan Plateau (TP) (e.g., Royden et al., 2008) and the eastward extrusion of lithospheric material. This motion is blocked by the South China block, leading to the remarkable clockwise rotation of the Sichuan-Yunan block (SYB) located on the SE margin of the TP, which is well captured by the Global Positioning System (GPS) velocity field (Fig. 1a, Wang and Shen, 2020;

Zheng et al., 2017). The SYB has experienced rapid uplift in the past 8–15 Ma and is considered to be the “youngest” development section of the TP, characterized by active seismicity and complex deformation patterns such as extension, shortening, and strike-slip (e.g., Guo et al., 2018; Lease et al., 2007; Royden et al., 2008).

The ~1000-km-long Red River fault (RRF), the west boundary of the SYB, is a profound structural discontinuity with a dextral slip rate of ~1.1 mm/yr (Shi et al., 2018). However, the low slip rate does not imply a low seismic potential. Both the 2008 Mw 7.9 Wenchuan earthquake (Zhang, 2013) and the 2021 Mw 7.4 Maduo earthquake (Guo et al., 2021a) occurred on the slowly deforming faults in China. The Weixi-

* Corresponding author at: Earth System Science Programme, The Chinese University of Hong Kong, Shatin, Hong Kong, China.

E-mail addresses: guorm@apm.ac.cn (R. Guo), hyang@cuhk.edu.hk (H. Yang).

<https://doi.org/10.1016/j.tecto.2023.229932>

Received 31 October 2022; Received in revised form 4 May 2023; Accepted 27 May 2023

Available online 5 June 2023

0040-1951/© 2023 Elsevier B.V. All rights reserved.

Qiaohou-Weishan fault (WQWF) is considered to be the northwestward extension of the RRF, whose length is about 280 km with a slip rate of 1.8–2.4 mm/yr (Chang et al., 2016). Several events with $M_s \geq 5.0$ occurred near the WQWF, and the recorded largest earthquake is the 1948 $M 6.3$ earthquake, but none of these historical earthquakes just fell on the geologically mapped fault line (Fig. 1c).

1.2. Overview of the 2021 Yangbi seismic sequence

At 21:48 on May 21, 2021, Beijing Standard Time (UTC Time 2021-05-21 13:48), a $M_s 6.4$ earthquake occurred in the Yangbi Country, Yunnan, China, resulting in 3 deaths and a large number of damage to local infrastructures. The China Earthquake Network Center (CENC) reported that the epicenter of the earthquake is located at 25.67°N, 99.87°E, with a depth of 8 km. The focal mechanism solution (Zhu et al.,

2022) shows that this event is dominated by the dextral movements with minor normal components (Fig. 1c), with a strike of 141° and a high dip of 83° towards the southwest. This event occurred ~15 km away from the WQWF, raising a question about the location of the seismogenic fault due to the absence of surface rupture.

The 2021 Yangbi earthquake was immediately preceded by a rich foreshock sequence. There are several large foreshocks of $M \geq 4.0$ within four days before the mainshock (Fig. 1c), including the largest $M_s 5.3$ foreshock. Foreshocks have been the proxy for examining the mainshock nucleation and growth (e.g., Huang et al., 2020; Kato and Ben-Zion, 2021). Up to date, triggering links between the major foreshocks and the Yangbi mainshock have been widely investigated. Stress transfer, aseismic slip, fluids, or a combination of them are invoked to explain the nucleation of the mainshock (e.g., Zhu et al., 2022; Liu et al., 2022a, 2022b; Sun et al., 2022; Zhang et al., 2021b; Yan et al., 2022; Zhou et al.,

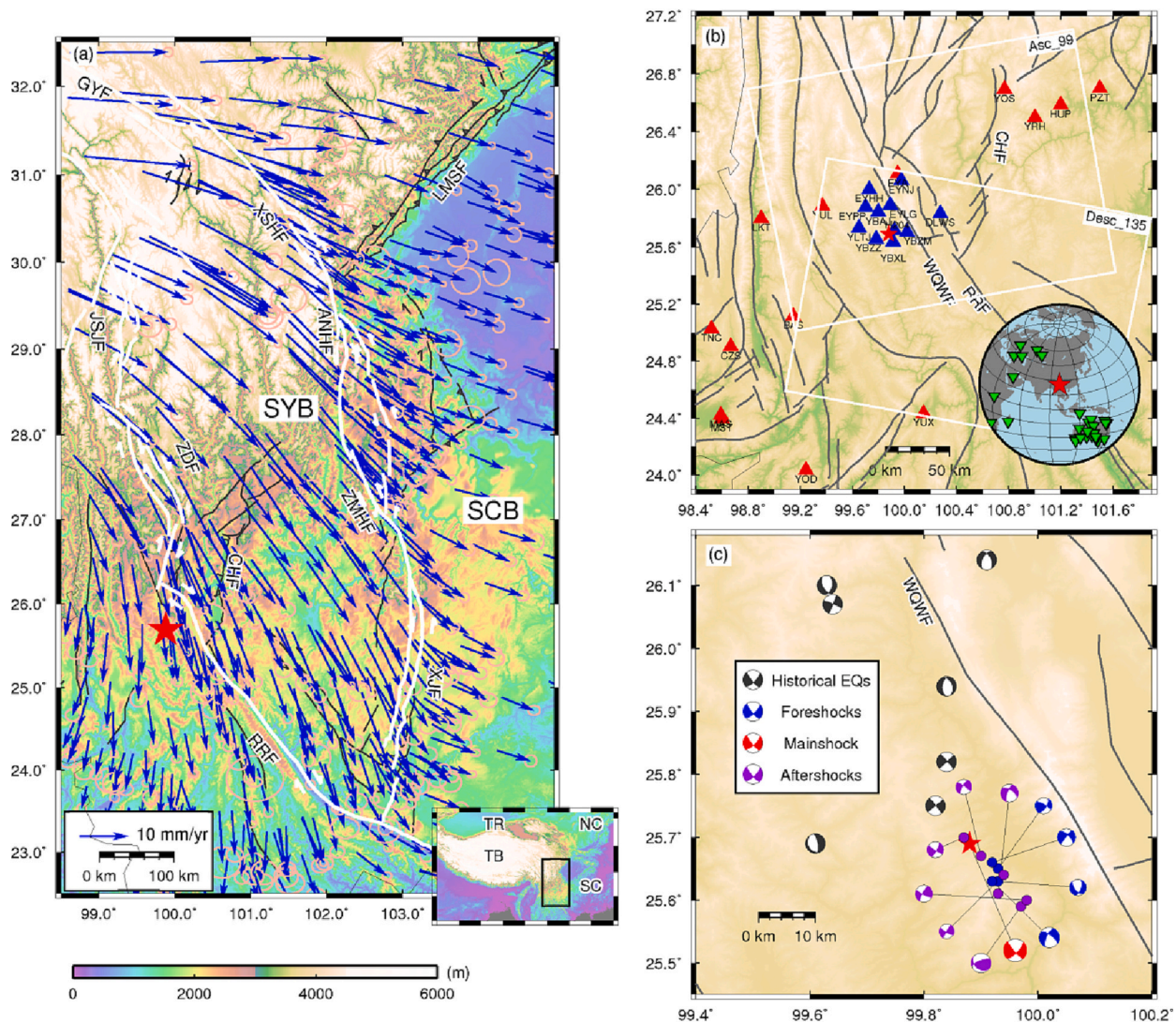


Fig. 1. Tectonic environment of the 2021 Yangbi source region. (a) The topography and GPS deformation in the southeastern Tibetan Plateau. The blue arrows represent the GPS surface deformation relative to the Eurasian plate from Wang and Shen (2020), and the pink ellipses represent the 98% confidence interval. The white lines represent the major faults around the Sichuan-Yunnan diamond-shaped block and the gray lines represent the other faults. The illustration in the lower right corner shows the large-scale background. (b) Data sets used in this work. Blue and red triangles are GPS sites and three-component seismic stations used in the coseismic slip inversion, respectively. Green inverted triangles represent teleseismic stations. White rectangles show the SAR coverage for ascending track 99 and descending track 135. (c) Focal mechanisms. Black beachballs indicate the focal mechanisms of historical earthquakes from the gCMT catalog (<https://www.globa.lcmt.org/>). Blue, red, and purple beachballs represent the focal mechanisms of foreshocks, mainshock, and aftershocks from Yang et al. (2021b), respectively. The red star is the epicenter of the Yangbi event. SCB: Sichuan Basin; SYB: Sichuan-Yunnan block; LMSF: Longmenshan fault; GYF: Ganzi-Yushu fault; XSHF: Xianshuihe fault; ANHF: Anninghe fault; ZMHF: Zemuhe fault; XJF: Xiaojiang fault; RRF: Red River fault; CHF: Chenghai fault; ZDF: Zhongdian fault; JSJF: Jinshajiang fault; TP: Tibetan Plateau; NC: North China; TB: Tarim Basin; SC: South China. WQWF: Weixi-Qiaohou-Weishan fault. (For interpretation of the references to colour in this figure legend, the reader is referred to the web version of this article.)

2022). Although a unified consensus has not yet been reached, this is not what we are studying in this work.

There also have been many aftershocks of magnitude 4 and 5, in which the Ms 5.0 and Ms 5.2 strong aftershocks occurred successively in 7 min and 36 min after the Ms 6.4 mainshock (Fig. 1c). The aftershock sequence is relatively abundant and distributed in an NW-SE trace about 27 km long, providing excellent prior information for mapping the hidden ruptured fault (Zhang et al., 2021b; Yan et al., 2022). Although the static dislocation distribution has been reported by some studies (e.g., Li et al., 2022; Liu et al., 2022; Xu et al., 2021; Wang et al., 2021), the spatiotemporal rupture of coseismic slip and the relationship between the mainshock, foreshocks, and aftershocks are still controversial, which can provide a key basis for understanding the seismogenic environment and accessing the future seismic potential in this region (Wang et al., 2022).

In this work, we try to resolve the detailed rupture process of the 2021 Ms 6.4 Yangbi earthquake by jointly using the teleseismic body waves, three-component regional observations, near-field GPS, and Interferometric Synthetic Aperture Radar (InSAR) data. The interplay between foreshocks, coseismic slips, and aftershocks can shed light on earthquake physics and future seismic hazards, which are also discussed. Finally, we analyze the stress and strain build-up pattern in the Yangbi source region and explain the reasons for the absence of strong earthquakes with $M \geq 6.5$ for decades here.

2. Seismic and geodetic data processing

The 2021 Ms 6.4 Yangbi earthquake has been well captured by the teleseismic P and SH waves, regional three-component waveforms, near-field GPS, and InSAR data (Fig. 1b). These well-documented dense networks provide an unprecedented opportunity to decipher the detailed spatial and temporal rupture process of the Yangbi event and understand the source characteristics of moderate earthquakes.

We select 14 P and 19 SH waveforms with a high signal-to-noise ratio (SNR), which are available in the Incorporated Research Institutions for

Seismology (IRIS) data management center (http://ds.iris.edu/wilber3/find_event). Their epicentral distance ranges from 30° to 90° to escape waveform complexities from the heterogeneity of crust and upper mantle at short distances and the core-mantle boundary at long distances (e.g., Guo et al., 2021b; Kumar et al., 2017). During the inversion, all teleseismic waveforms are deconvolved to velocities at a sampling rate of 0.2 s and bandpass filtered at 0.002–0.5 Hz. In addition, we set the weight of P waves twice that of SH waves, because the P wave decays slower with distance than the SH wave, and it is also easier to pick the first motion. The generalized ray theory and reflection and refraction method are applied to compute the teleseismic Green's functions (Helmberger, 1974).

We collect 14 three-component regional waveforms with high SNRs from the China National Digital Seismic Network (<https://doi.org/10.7914/SN/CD>) and the Institute of Engineering Mechanics, China Earthquake Administration (<https://data.earthquake.cn/datashare/report.shtml?PAGEID=datasourcelist&dt=ff80808277cc56050179c55ee7220005>). The accelerograms are bandpass filtered with a frequency band of 0.02–0.5 Hz to prevent the contamination of long-period integration noise and the inadequacy of the theoretical Green's function at higher frequencies (Liu et al., 2015). Then they are integrated to the ground velocities. During the inversion, each component of every station is given the same weight. The regional Green's functions are calculated by the frequency-wavenumber integration method (Zhu and Rivera, 2002).

There is a continuous GPS dense array in the ~ 50 -km area centered on Eryuan County, composed of 34 stations that were successively completed between March 2018 and July 2020 (Fig. 2). The Yangbi earthquake occurred south of this GPS network, whose coseismic deformation was well captured by this array. The specific GPS data processing please refers to Text S1. We select 11 GPS stations with significant coseismic displacement signals and good azimuth to participate in the joint inversion (Figs. 1b and 3). Given the low SNRs and large uncertainties of most vertical GPS components, we use only horizontal GPS displacements, except for the station YBXL with the maximum

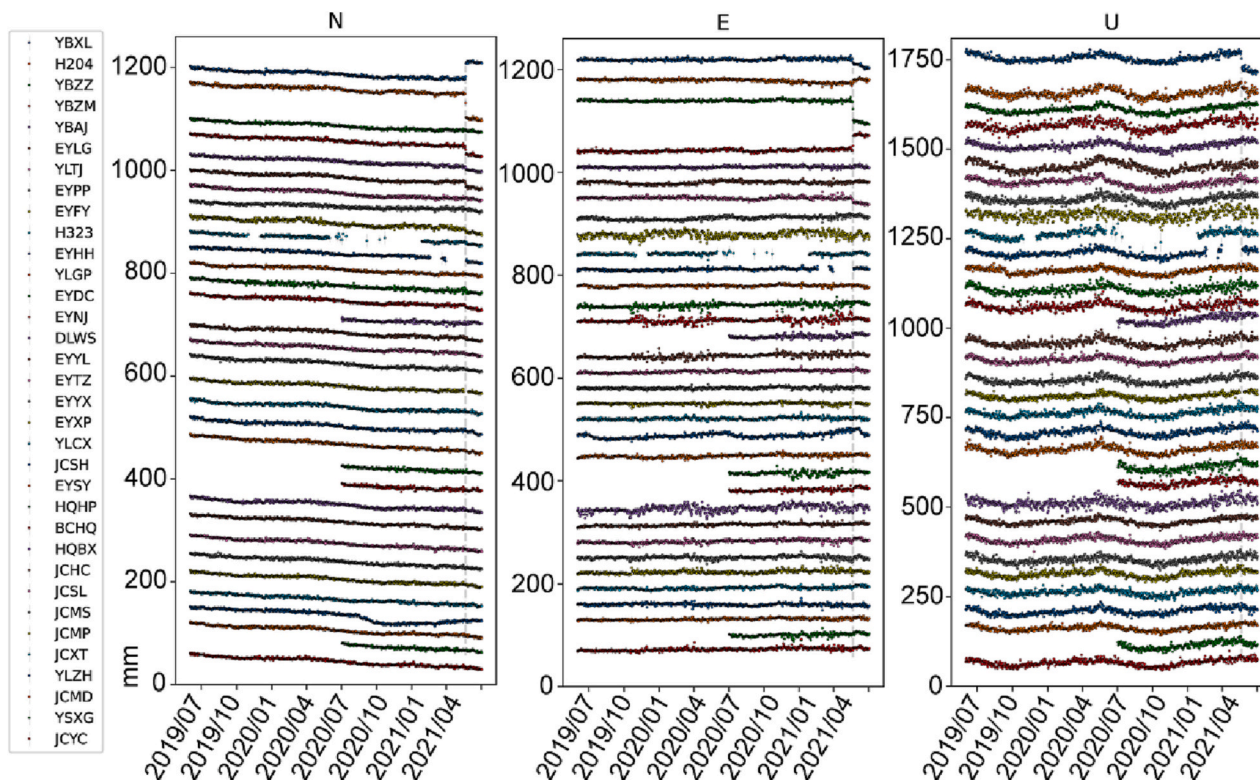


Fig. 2. Time series on each GPS site.

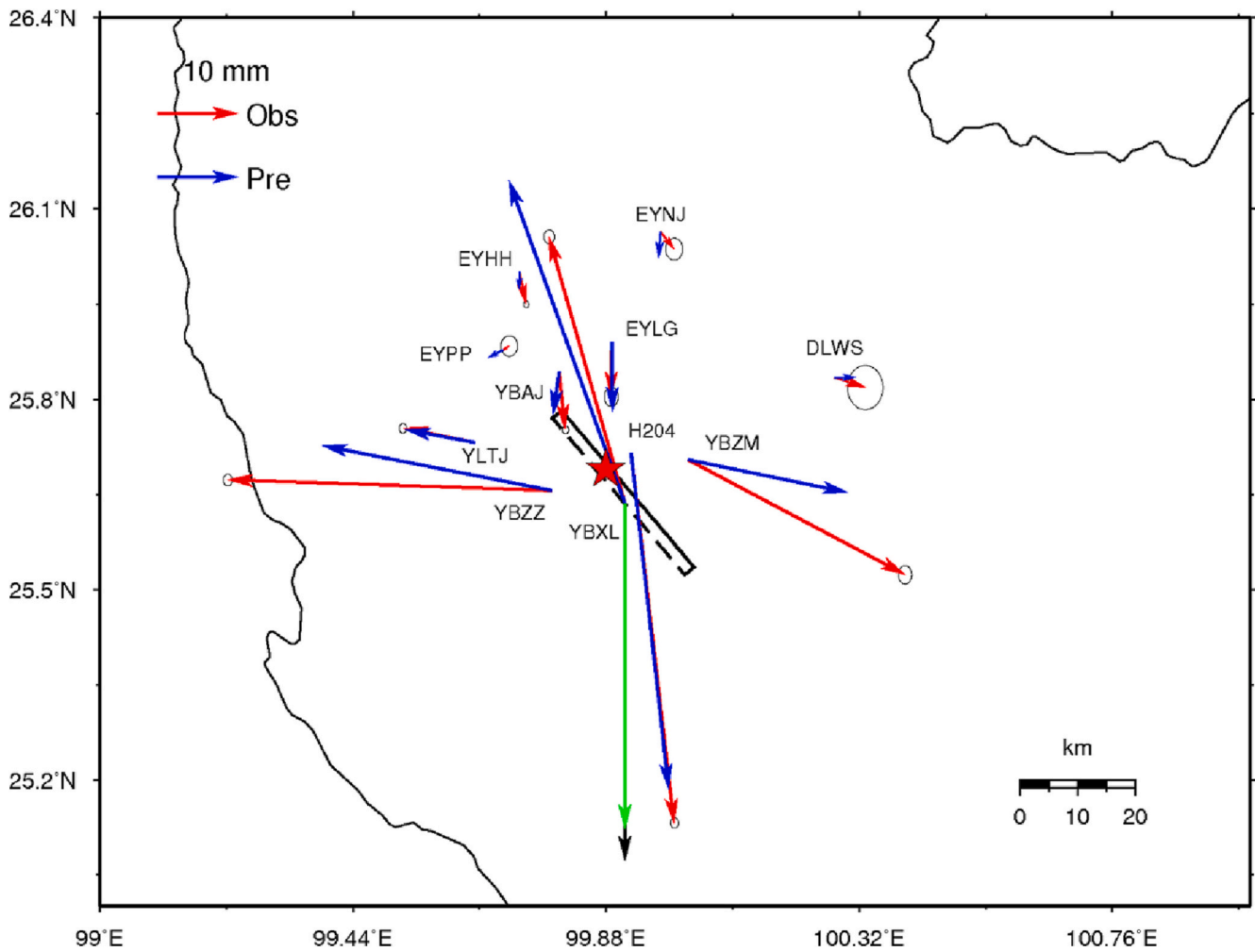


Fig. 3. Comparison between the observed and predicted GPS displacements. Red and blue lines are the horizontal GPS observations and predictions, respectively. Black and green lines are the vertical GPS observations and predictions, respectively. The dashed rectangle presents the surface projection of the fault plane, and the thick line is the fault trace. The red star is the epicenter of the 2021 Yangbi event. (For interpretation of the references to colour in this figure legend, the reader is referred to the web version of this article.)

subsidence of ~ 44 mm. As shown in Fig. 3, the marked horizontal displacements are mainly observed within the range of ~ 50 km from the epicentral distance, and their magnitude decays rapidly as the epicentral distance increases. The four stations with the largest horizontal displacements appear in different patterns: station H204, located ~ 5.3 km NE of the epicenter, moves ~ 46.1 mm to the south; station YBXL, located ~ 6.9 km SE of the epicenter; moves ~ 34.3 mm to the north; the station YBZZ, located ~ 10.2 km W of the epicenter, moves ~ 40.0 mm to the west; and the station YBZM, located ~ 14.3 km E of the epicenter, moves ~ 30.4 mm to the east. It reveals that the seismogenic fault passes through the middle of sites H204 and YBXL, imposing a strong constraint on the fault geometry. During the inversion, the weight of each station is set to be equal. We calculate the static Green's functions using the generalized reflection-transmission coefficient matrix method (Xie and Yao, 1989).

We employ the two-pass method of differential interferometry to derive coseismic deformation associated with the 2021 Yangbi earthquake. The Sentinel-1 SAR images with descending and ascending orbits (Table S1) are provided by the European Space Agency (ESA). The data processing is performed based on the open-source GMTSAR software (Sandwell et al., 2011). The 30 m resolution digital elevation model from NASA Shuttle Radar Topography Mission (SRTM) is applied to eliminate topographical effects. To improve the interferometric coherence, the interferograms are multiviewed with a factor of 8:2 and

filtered using a Gaussian filter with 200 m wavelength (Goldstein and Werner, 1998). The SNAPHU software (Chen and Zebker, 2001) is invoked to phase unwrapping. The tropospheric delay is calibrated by using the Generic Atmospheric Correction Online Service (GACOS) (e.g., Yu et al., 2018). After geocoding, the ascending and descending line-of-sight (LOS) deformation associated with the Yangbi event is obtained.

3. Inversion methodology and model setup

In this work, we apply a joint finite fault inversion algorithm of Ji et al. (2002) to simultaneously invert the average rupture speed, rise time, rake angle, and slip amplitude of the 2021 Yangbi earthquake. This method performs the inversion in the wavelet domain, which can combine the seismic and geodetic observations to decipher the detailed source characteristics. It has been extensively invoked to recover the rupture processes of some major earthquakes (e.g., Chousianitis and Konca, 2021; Guo et al., 2020a; Wang et al., 2018). The kinematic slip model can be derived by minimizing the objective function, which is defined by incorporating the misfits of waveforms and geodetic observations, as well as the fault slip and seismic moment smoothness constraint, as follows

$$misfit = e_{wf} + w_{static}e_{static} + w_{slip}\Delta_{slip} + w_{sm}\Delta_{sm} \quad (1)$$

Where e_{wf} is the misfit between the seismic observations and

predictions, including the teleseismic body waves and regional three-component waveforms. e_{static} is the misfit between the observed and predicted GNSS and InSAR data. Δ_{slip} and Δ_{sm} represent the slip difference between adjacent subfaults and the discrepancy between the modeled and referenced seismic moments, respectively. Parameters w_{static} , w_{slip} , w_{sm} denote the relative weighting of the geodetic misfit, the Laplacian slip smoothness, and the seismic moment constraint, respectively (Ji et al., 2002). Given that reasonable variations of relative weighting do not induce significant differences in the data fits and slip pattern (e.g., Wang et al., 2018; Yue et al., 2014), they are set to 1.0, 0.1, 0.1 following previous studies (Guo et al., 2019; Ji et al., 2002; Wang et al., 2018), respectively.

During the inversion, we need to impose a priori information about the fault geometry and rupture initiation. Based on the relocated foreshocks and aftershocks (Yang et al., 2021a; Zhang et al., 2021a), the fault strike and dip angles are set as 140° and 84° , respectively, compatible with the point-source mechanism solution of the mainshock (G. Zhu et al., 2022) and the symmetrical ground motion pattern (X. Liu et al., 2022). Different relocation results derive a similar epicenter, providing a perfect constraint on the hypocenter location at 25.69°N , 99.88°E (Su et al., 2021; Yang et al., 2021a; Zhang et al., 2021a). Because the teleseismic depth phases pP and sP are sensitive to the source depth (e.g., Xie et al., 2013), the differential travel times between P-pP and P-sP (Heyburn et al., 2013) are used to determine the initial rupture depth of the 2021 Yangbi earthquake. As shown in Fig. 4, the optimal source depth is ~ 7.6 km. The average rupture speed is limited to 2.2 km/s, consistent with the models of Gong et al. (2022) and Chen et al. (2022). In addition, several constraints are applied to make the inversion more stable: a seismic moment of 1.74×10^{18} N-m (Mw 6.1)

from the USGS solution is applied as the reference moment; the rupture speed is constrained from 1.0 to 3.0 km/s; the rise time of each patch varies between 0.8 s and 4.0 s; the rake angle is allowed to vary from -250° to -110° ; and the maximum slip is not allowed to exceed 1.5 m. To recover the detailed rupture features, the rectangular fault plane is gridded into some small patches of 2 km by 2 km, spanning 36 km along strike and 20 km along dip. It allows the coseismic slip to rupture to the ground. Moreover, we apply the same 1-D velocity model as Zhang et al. (2021a) and Zhu et al. (2022) when calculating Green's functions.

4. Results and discussion

4.1. Kinematic source characteristics

The detailed kinematic rupture process of the Ms 6.4 Yangbi earthquake is visualized in Fig. 5, and its surface projection is demonstrated in Fig. S1. The primary slip is concentrated in an asperity at a depth ranging between 5 km and 13 km, which is dominated by the dextral movements with a small percentage of normal components. No surface rupture occurred in the Yangbi earthquake, as indicated by the continuity striations in the radar interferogram (Liu et al., 2022) and confirmed by field investigations (Li et al., 2021). The peak slip is ~ 0.8 m at a depth of ~ 7.3 km along dip (Fig. 5a). The released seismic moment is approximately 1.7×10^{18} N-m (Mw 6.1), similar to the gCMT point-source solution (1.6×10^{18} N-m).

Fig. 6 demonstrates snapshots of the rupture expansion from our optimal slip distribution, revealing a unilateral rupture propagation dominated by southeastward expansion, spanning ~ 12 km along strike. The rupture initiates at the hypocenter and then expands as a slip-pulse. The released seismic moment rate rapidly increases at the first ~ 6 s and reaches the peak value of $\sim 3.0 \times 10^{17}$ N-m/s, then it decreases gradually with time (Fig. 5d). Fig. 5b illustrates the spatial distribution of rise time for each subfault (the slip of 0.15 m is set as the cutoff threshold), revealing a heterogeneous pattern. The slip rate is specified as the ratio of slip to the rise time, whose peak value is about 1.0 m/s (Fig. 5c).

The associated teleseismic body waves and regional three-component waveforms data fits are depicted in Figs. 7 and 8, respectively. Although most of the seismograms are well recovered, some mismatches could be seen, which may be attributed to the effects of 3-D complex crustal structure. Moreover, our optimal slip model can effectively reproduce the InSAR observations (Fig. 9), except for the northeast disk of the ascending orbit, attributed to the atmospheric delay interference that is difficult to eliminate (Xu et al., 2021). For more details of cumulative coseismic GPS observations and predictions, please see Table S2 and Fig. 3. Generally, our slip model can well explain the static GPS displacements, although there are some small fitting errors at some stations, such as the YBZM and YBZZ sites. Both of them with "relatively large" horizontal displacements may be related to the loose soil or landslides beneath the stations, pending further field investigation (Zhang et al., 2021a).

4.2. Comparison with previous studies

There is a consensus on two features of the slip model associated with the 2021 Yangbi event: one is unilateral rupture along strike; the other is that the coseismic slip does not reach the surface (e.g., Gong et al., 2022; Zhang et al., 2021a; Li et al., 2022; Liu et al., 2022; Xu et al., 2021; Wang et al., 2021), consistent with our model results. However, there are discrepancies in the rupture direction along dip, the peak slip (Gong et al., 2022), and the high-slip coseismic asperity. The finite fault results using the apparent moment-rate functions from Gong et al. (2022) revealed that the rupture propagates downdip, while the rupture process from Chen et al. (2022) showed a feature propagating upward from the hypocenter of 11 km. The difference is that our results imply near-horizontal propagation along strike. Most of the static coseismic slip distribution derived from the GPS and/or InSAR data (Zhang et al.,

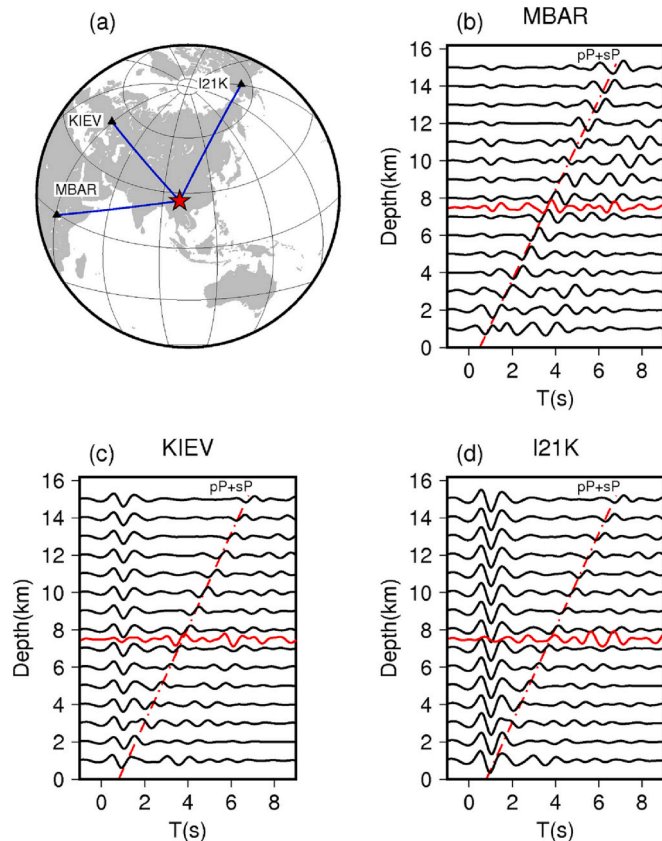


Fig. 4. Hypocentral depth of the 2021 Yangbi earthquake. (a) Stations distribution. (b), (c), and (d) show the comparison of the observed (red) and synthetic (black) waveform (black) for MBAR, KIEV, and I21K sites, respectively. (For interpretation of the references to colour in this figure legend, the reader is referred to the web version of this article.)

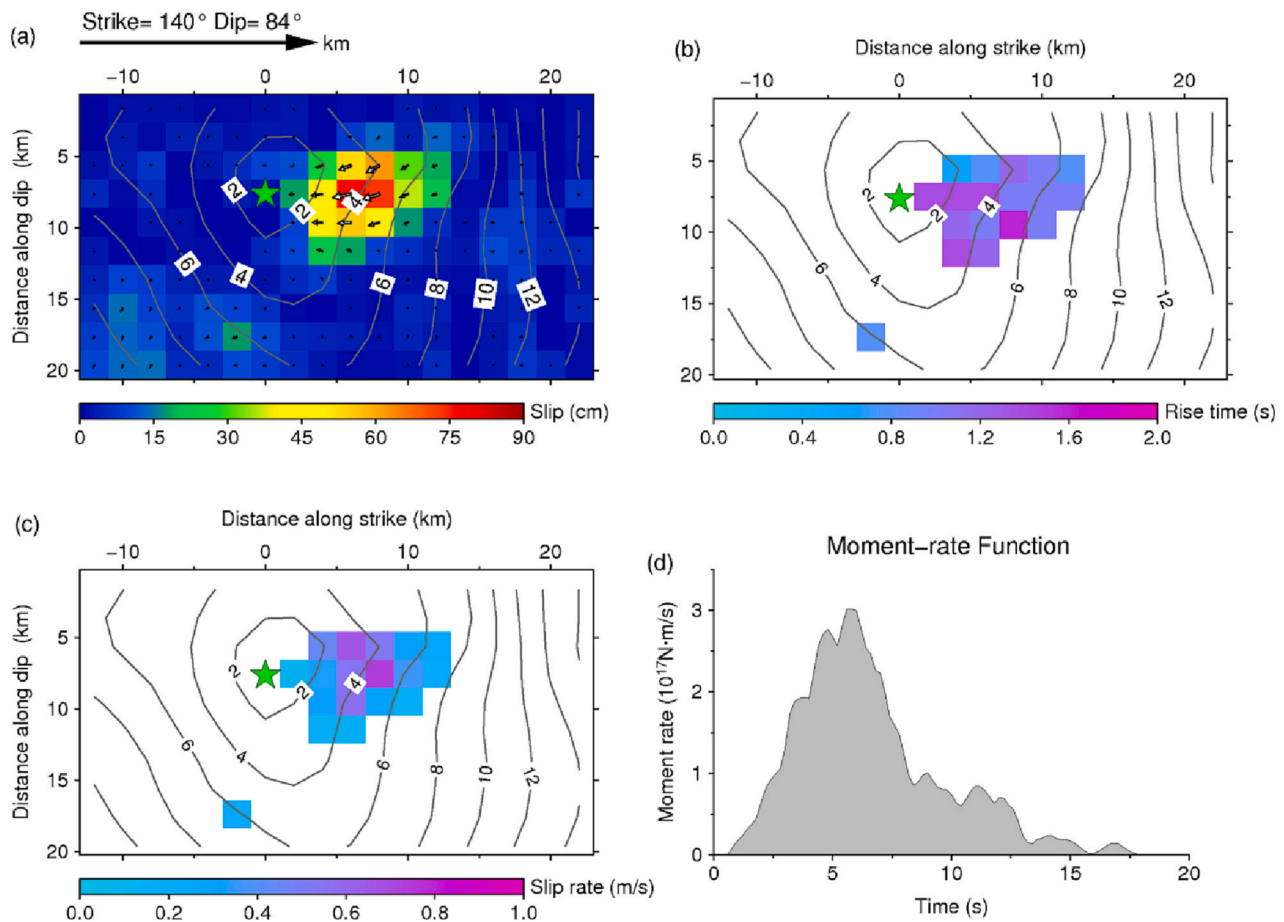


Fig. 5. The optimal rupture process of the 2021 Yangbi earthquake. (a) Slip distribution from our preferred model. White arrows denote the rake angles and relative sizes of slip. Distribution of (b) rise time and (c) slip rate. Subfaults with slip <0.15 m are excluded. (d) Moment rate function. Gray contours represent the rupture propagation time in seconds. The green star is the hypocenter of the Yangbi event. (For interpretation of the references to colour in this figure legend, the reader is referred to the web version of this article.)

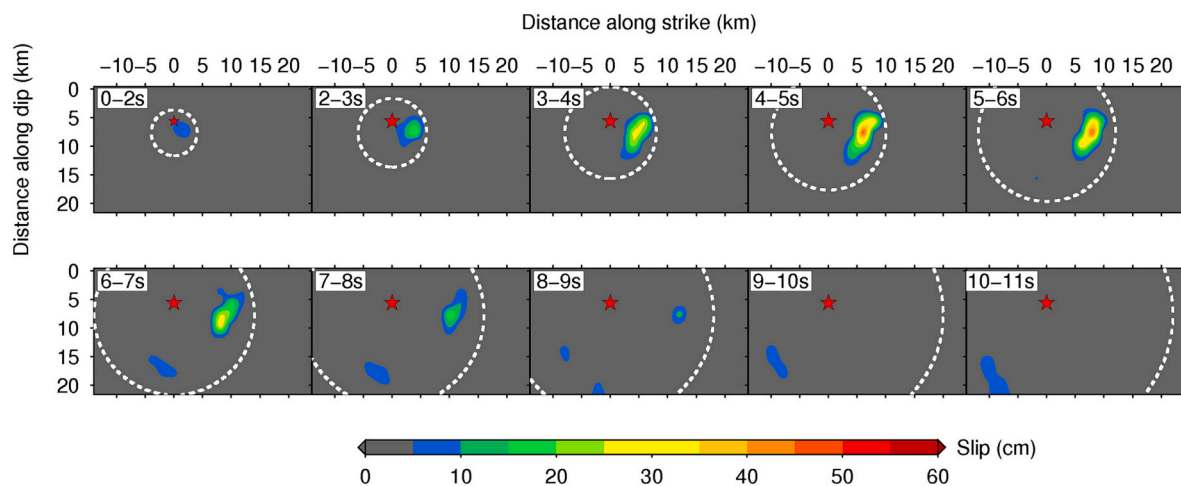


Fig. 6. Snapshots of the rupture expansion history every one second for the 2021 Yangbi earthquake. Colors shading denotes the fault slip average over 1 s interval. The white dashed contour presents the pseudo-rupture front with a rupture speed of 2.0 km/s. The small slip after 11 s is considered to be unreliable.

2021a; Li et al., 2022; Liu et al., 2022; Xu et al., 2021) exhibited a relatively large asperity, distributed over a range of approximately 2–14 km, with a peak slip of <1 m. A concentrated high-slip area (7–12 km) was obtained by Gong et al. (2022), but its peak exceeded 2 m. In our preferred model, the coseismic asperity is constrained by a relatively narrow zone (5–13 km), and the peak slip is moderate.

4.3. Shallow slip deficit due to fault immaturity

The phenomenon of shallow slip deficit (SSD) has been documented in many strike-slip events (Fig. 10), in which the maximum coseismic slip is concentrated in the middle of the brittle crust and decreases towards the surface (C. Liu et al., 2021). A significant SSD associated with

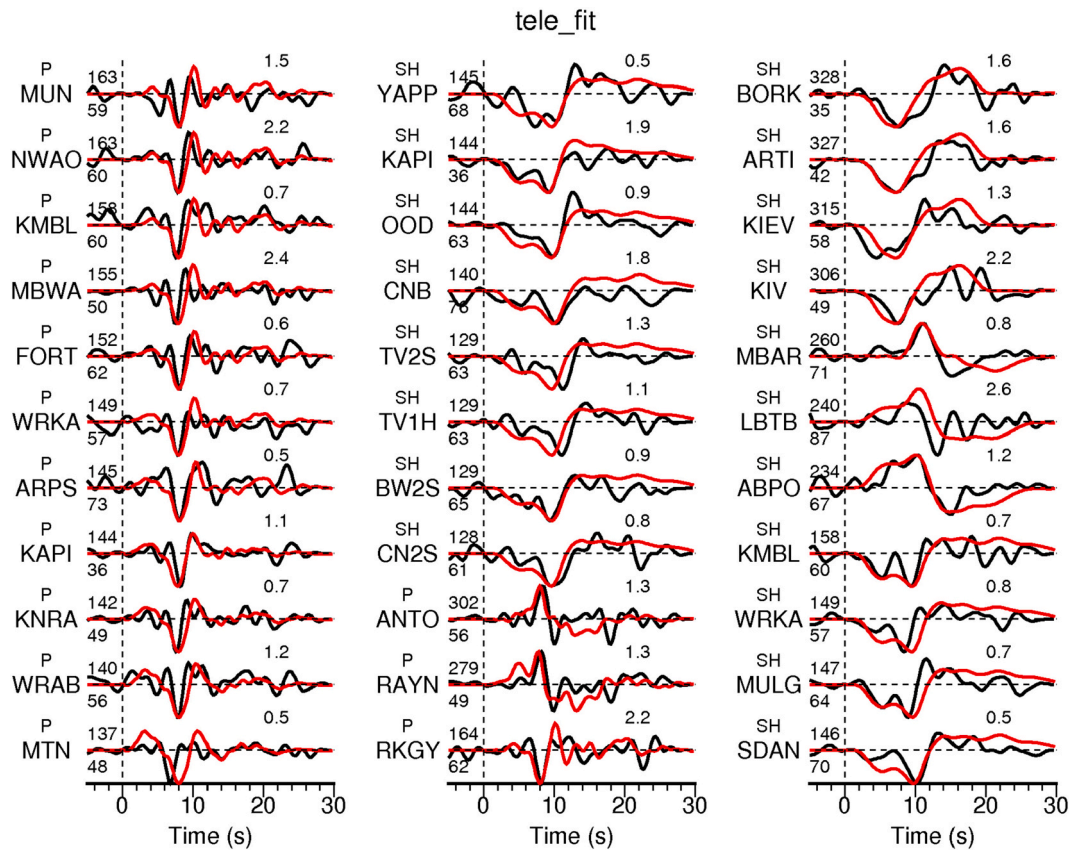


Fig. 7. Comparison of teleseismic observed (black lines) and predicted (red lines) waves, involving 14 P waves and 19 SH waves. The azimuth and distance in degree are stated at the beginning of each wave with the distance at the bottom. And the station name and peak velocity are located at the beginning and end of each wave, respectively. (For interpretation of the references to colour in this figure legend, the reader is referred to the web version of this article.)

the Yangbi earthquake is also observed in the top 0–5 km of the crust (Fig. 5a). One understanding of the slip termination in the uppermost crust is the presence of velocity-strengthening fault friction at shallow depths, with SSD compensated by interseismic creep and/or postseismic afterslip (e.g., Fialko et al., 2005; Yue et al., 2017; Yang and Yao, 2021). However, many seismic events with SSD are not associated with either resolvable shallow interseismic creep or robust shallow afterslip (Kaneko and Fialko, 2011; Sadeghi Chorsi et al., 2022). Geodetic observations reveal that both of them are rather uncommon at shallow depths (e.g., Fialko, 2004; Kaneko and Fialko, 2011), especially for infrequent and immature sliding faults (Fialko et al., 2005), except for certain regions near major creeping parts of mature faults and/or areas with thick sedimentary overburden of overpressured pore fluids (e.g., Wei et al., 2009). Therefore, neither shallow creeping nor afterslip can be used to fully explain the origin of the SSD (Yang and Yao, 2021).

SSD is especially severe for immature faults (Sadeghi Chorsi et al., 2022). Fault structural maturity, that is, the sliding longevity of a fault, greatly affects the behavior of earthquakes (Choy and Kirby, 2004; Manighetti et al., 2007, 2015, 2021; Wesnousky, 1988). The Yangbi earthquake occurred on a blind fault system with some conjugate aftershock trends, stepovers, and parallel strands (Gong et al., 2022; Lei et al., 2021; Liu et al., 2022b; Su et al., 2021), similar to the 2013 Eryuan (Liu et al., 2022a) and 2019 Ridgecrest sequences that occurred on an immature fault system (Barnhart et al., 2020; Feng and Almeida, 2020; Goldberg et al., 2020). In general, large earthquakes with fast rupture rates and long propagation distances are more likely to occur on smooth and simple mature faults, while immature faults are prone to produce more frequent, smaller magnitude earthquakes because they are separated by stepovers and higher strength barriers (e.g., Manighetti et al., 2021; Perrin et al., 2016; Thakur and Huang, 2021). In addition, the low

average rupture speed and small moment scaled radiated energy of the Yangbi earthquake are compatible with the high fracture energy dissipation of immature faults (Gong et al., 2022). Note that the immature strike-slip fault has the potential to produce the supershear rupture, such as the seismogenic fault of the 2021 Maduo earthquake (Cheng et al., 2023). Combined with the rupture features, low fault slip rate (Chang et al., 2016; Shi et al., 2018; Shen et al., 2005), complex fault structure (Shi et al., 2018; Wen et al., 2022), and distributed deformation pattern in the source region (discussed in Section 4.5), we argue that the seismogenic fault of the 2021 Yangbi event is immature (Lei et al., 2021). SSD on such faults could be possibly compensated by distributed inelastic deformation during the interseismic period (e.g., Barnhart et al., 2020; Feng and Almeida, 2020; Fialko et al., 2005; Kaneko and Fialko, 2011). Similar inferences were drawn for the 2003 Mw 6.5 Bam earthquake (Fialko et al., 2005) and the 2020 Mw 6.8 Elazığ earthquake (Galović et al., 2020). The long-term non-brittle fault behavior of the uppermost crust is widely recognized in field studies of thrust tectonics (Dolan et al., 2003). For strike-slip faults, the uppermost crust may also be characterized by inelastic deformation due to granular flow, folding, or some other distributed damage mechanism (Fialko et al., 2005). It is important to note that here we cannot exclude the possibility that the SSD is caused by the shallow crust being locked.

4.4. Interplay between the coseismic slips, foreshocks, and aftershocks

As shown in Fig. 11c, the coseismic slips and aftershock loci are found to be complementary, which has been observed by other large earthquakes, for example, the 2015 Mw Illapel, Chile, earthquake (e.g., Melgar et al., 2016), the 2016 Mw 7.0 Kumamoto, Japan, earthquake (e.g., Yue et al., 2017), and the 2017 Mw 8.2 Chiapas, Mexico, earthquake

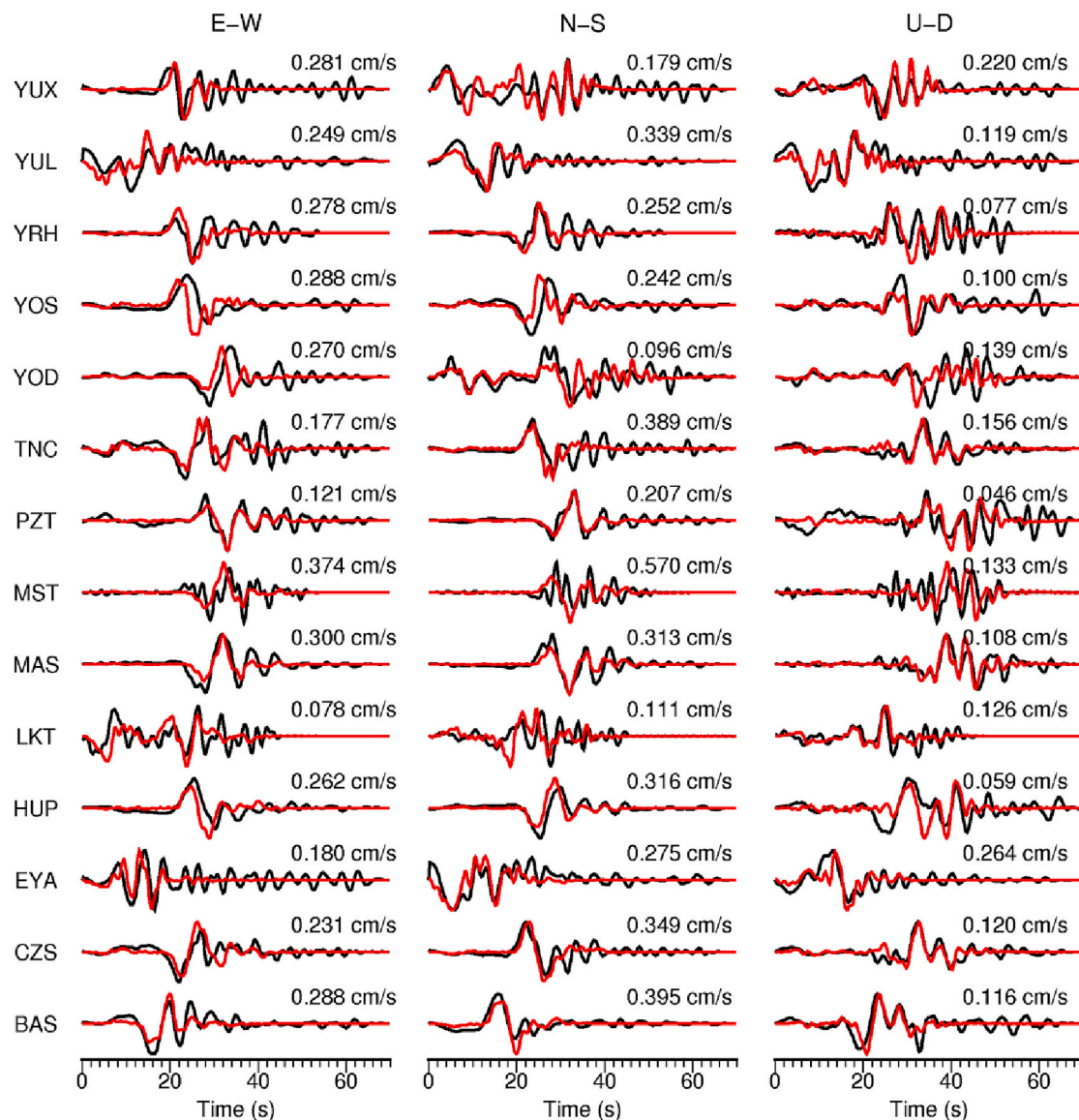


Fig. 8. Comparison of three-component regional observations (black lines) and predictions (red lines). The station names are at the beginning of each seismogram, and the peak velocity of each record is at the right top. (For interpretation of the references to colour in this figure legend, the reader is referred to the web version of this article.)

(e.g., Guo et al., 2019). The coseismic high-slip region is depleted of aftershocks, and aftershocks are mainly concentrated in the flanks of the significant coseismic slips at shallower depths from 3 to 6 km (Fig. 11c), indicating that the strain energy in the asperity has been sufficiently released by the mainshock. Under the assumption that aftershocks directly induced by coseismic stress change only occur in the early postseismic phase (the first hours after the mainshock), aftershocks complementary to the coseismic slips can be understood as ruptures that occurred on the velocity-strengthening creeping zones (Perfettini and Avouac, 2007; Perfettini et al., 2018; Yue et al., 2017). For this mechanism, the coseismic slips usually transfer significant Coulomb stress increase to the nearby brittle creeping zones (Fig. 11d), but the surrounding velocity-strengthening zones could hinder the coseismic rupture. During the postseismic period, the creeping zones loaded by the mainshock would experience some aseismic afterslip, in line with the framework of the stress-driven afterslip model (e.g., Barbot et al., 2009; Johnson et al., 2006). And with the rapid accumulation of afterslip, aftershocks are produced accordingly (e.g., Lange et al., 2014; Perfettini et al., 2018).

As shown in Fig. 11c, foreshocks are mainly distributed in the updip

of the coseismic slips, where there are only a few aftershocks (Zhou et al., 2021). And most foreshocks and aftershocks, as well as the mainshock are located linearly on a SE-trending fault plane. Therefore, the slip of foreshocks fills the slip deficit of the mainshock and aftershocks, and jointly releases the accumulated energy of the fault plane during the interseismic period. Zhu et al. (2022) detected the spatio-temporal migration of the foreshock sequence to the hypocenter, which can well resolve the relationship between foreshocks and the initiation of the mainshock rupture process. The rupture zones of most large foreshocks are adjacent with little overlap, and the mainshock is ultimately initiated at the edge of the foreshock rupture zone, where there is a localized increase in shear stress, coinciding with a triggered cascading stress transfer. Thus, foreshocks, coseismic slips of the mainshock, and aftershocks in the Yangbi seismic sequence form a complementary pattern in accordance with the Coulomb stress triggering relationship.

4.5. Diffuse strain rates in the northern region of the RRF

Rock mechanics (e.g., Hamiel et al., 2004) and simulations of evolving seismicity (e.g., Lyakhovskiy and Ben-Zion, 2009) suggest that

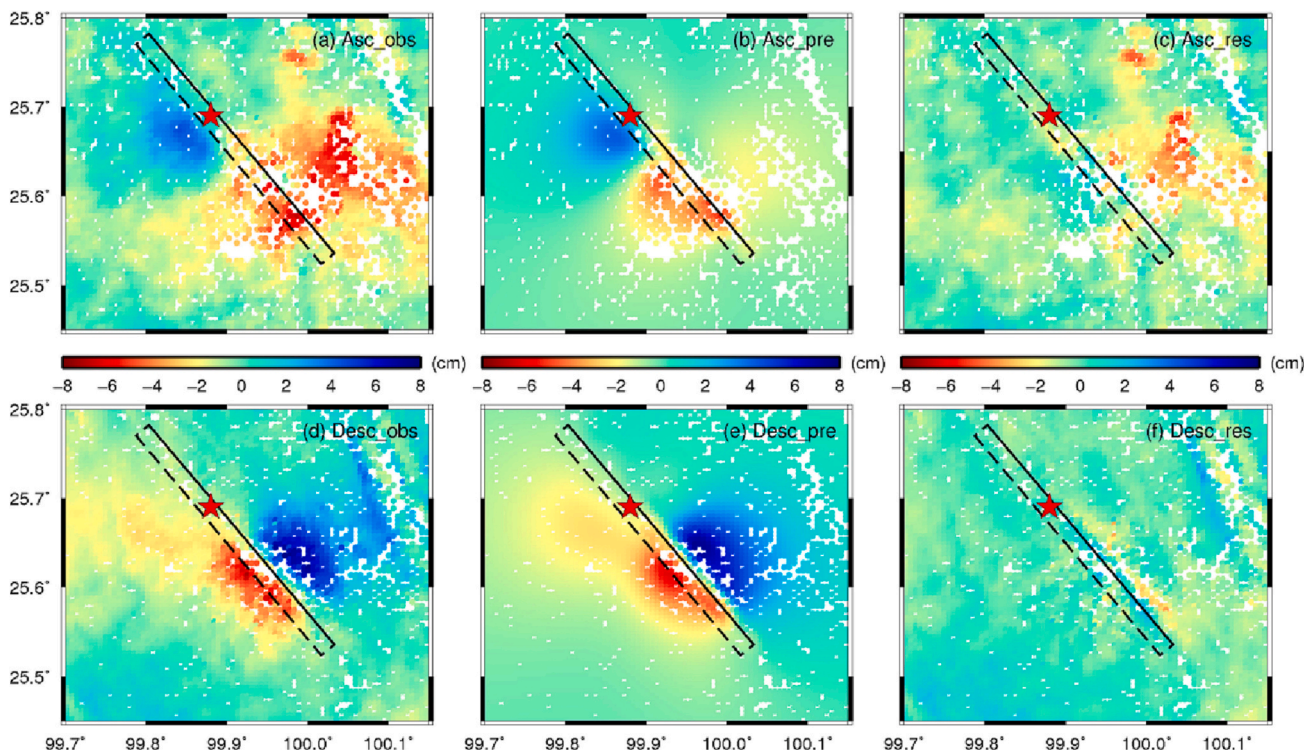


Fig. 9. InSAR data fitting. Observed and predicted Sentinel (a–b) ascending and (d–e) descending InSAR data. (c) and (f) indicate the residuals between the observations and predictions of ascending and descending InSAR data, respectively. The dashed rectangle denotes the surface projection of the fault plane, and the thick line is the fault trace. The red star is the epicenter of the 2021 Yangbi event. (For interpretation of the references to colour in this figure legend, the reader is referred to the web version of this article.)

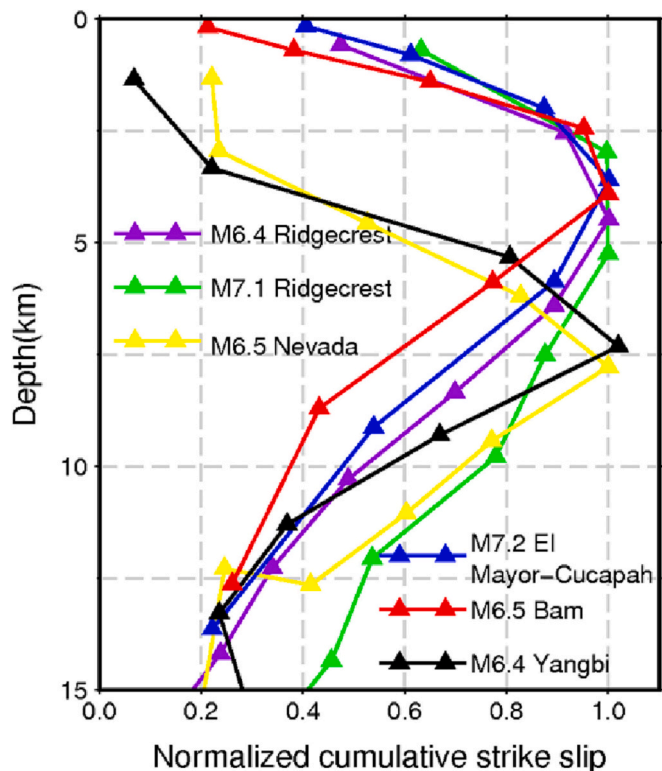


Fig. 10. Normalized cumulative coseismic slip versus depth for the Ms 6.4 Yangbi earthquake (solid black line) and several major strike-slip earthquakes (Liu et al., 2021).

the evolution of a seismic cycle goes through three steps: (1) accumulation phase, (2) localization phase, and (3) rupture phase. Seismic observations reveal that the elastic stresses are released near the rupture source after a major earthquake, causing a stress shadow (Freed et al., 2007; Guo et al., 2020b; Kroll et al., 2017; Simpson and Reasenber, 1994). Diffuse deformation and smaller events are widely distributed (accumulation phase). Then, the stresses gradually evolve out of the shadow and reorganize along the main fault system, accompanied by changes in the location of seismic activity and deformation pattern (localization phase). When the stress reaches a critical threshold of the maximum frictional resistance, another large earthquake occurs (rupture phase). Given the time-dependent patterns, we are able to identify the phase of the interseismic period in our study region based on the strain rate and earthquake distribution to assess the seismic hazard in the near future (e.g., Shen et al., 2007; Zeng et al., 2018).

In this study, we estimate strain rate partitioning based on the interseismic GPS surface velocities from our new-built GPS stations (Table S3) and Wang and Shen (2020) (Figs. 2 and 12) and download the earthquakes with $M \geq 4.5$ from 1976 to 2020 from the gCMT project. The method proposed by Shen et al. (2015) is invoked to derive the continuum strain rate field. The detailed description please refers to Text S2. As shown in Fig. 13c, the northern region of the RRF has good spatial resolutions. Fig. 13a shows the horizontal strain rate field, where the background represents the maximum shear strain rate, and the maximum and minimum principal strain rate tensors are plotted as conjugate vector pairs. The second invariant of horizontal strain rates demonstrates a similar pattern (Fig. 12). Fig. 13b demonstrates the distribution of dilatation rates, corroborated by the focal mechanisms of historical events. The source region of the Yangbi earthquake is characterized by shear strain rates with very minor contraction strain rates (Fig. 13), cohere with the coseismic slips of the Yangbi event (Fig. 5). Both high shear and contraction strain rates are mainly concentrated west of the Chenghai fault. While the maximum extensional dilatation is

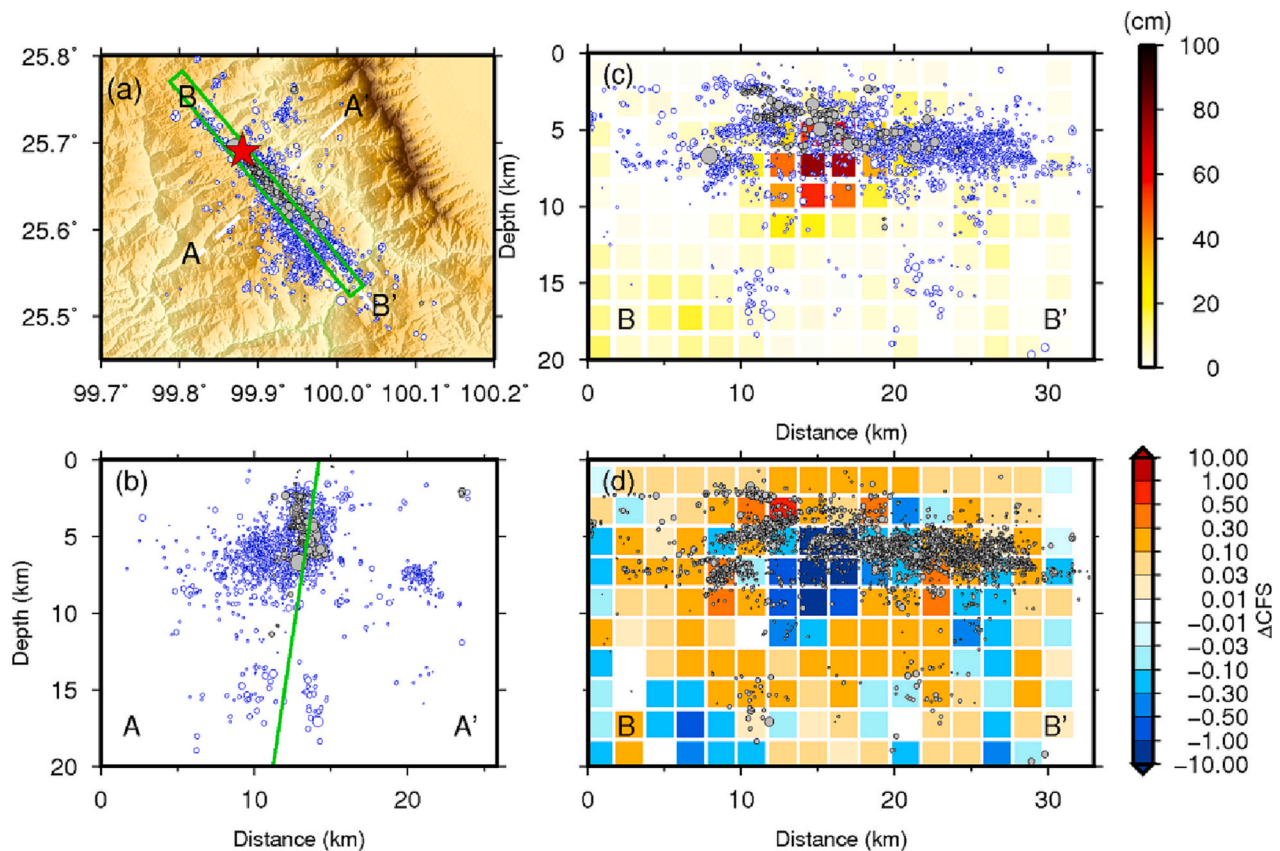


Fig. 11. Complementary pattern between foreshocks, coseismic slips, and aftershocks. (a) Distribution of relocated foreshocks and aftershocks. Relocated foreshocks (white circles with blue borders) and aftershocks (gray circles with gray borders) are from the work of Zhou et al. (2021). The red star is the epicenter of the Yangbi earthquake. The green rectangle is the surface projection of the seismogenic fault. The aftershocks along the cross sections (b) AA' and (c) BB'. The green line is the seismogenic fault. The slip distribution is red-coded. The pink shadows demonstrate the region with a shallow slip deficit. (d) Δ CFS triggered by the mainshock along the cross section of BB' in MPa. (For interpretation of the references to colour in this figure legend, the reader is referred to the web version of this article.)

distributed near the Jianchuan-Qiaohou fault. Overall, the high strain rates are not localized along the main faults, but are diffused in the northern region of the RRF (Li et al., 2020; Wen et al., 2022).

As illustrated in Fig. 13b, earthquakes of $M \geq 4.5$ are also dispersed and widely distributed in both high and low strain rate regions, implying that the northern region of the RRF is in the accumulation phase during the interseismic period. The absence of large events with $M \geq 6.5$ for decades also confirms this. The wide distribution of seismicity and strain rate may be due to the stress shadow of previous large earthquakes (Simpson and Reasenber, 1994; Zeng et al., 2018). The size of the stress shadow is controversial, but the region may be quite large considering the viscoelastic behavior of the lower crust and upper mantle (Pollitz et al., 2008). Stress shadows from the 1515 $M7^{3/4}$ Yongsheng event (Luo et al., 2015) and the 1925 $M7.0$ Dali earthquake reduced stresses across the region. These stress reductions led to the extensive deformation and dispersed seismicity in the northern region of the RRF. During this period, stresses and strains accumulate over a wide area around the fault, resulting in small-scale fractures distributed throughout the region (Zeng et al., 2018), compatible with the small-scale fault spacing and diffuse deformation in the southeastern TP (e.g., Bai et al., 2010; Yang et al., 2020; Li et al., 2020; Wen et al., 2022). Therefore, we argue that the northern region of the RRF is less likely to have a major earthquake with $M > 6.5$ in the near future.

5. Conclusions

In this study, the kinematic rupture process of the 2021 Yangbi earthquake is inverted by the teleseismic P and SH waves, three-component regional waves, GPS, and InSAR observations. The joint

inversion results show that the pulse-like rupture is concentrated in an asperity at depths of 3–13 km, propagating towards SE with a peak slip of ~ 0.8 m at the depth of ~ 7.3 km. The shallow slip deficit is due to the distributed inelastic deformation that occurs predominantly during the interseismic period. The foreshocks, coseismic high-slip zone, and aftershocks form a detailed complementary pattern, in line with the triggered interplay of stress transfer. Both the diffused strain rate and seismicity present the accumulation phase of the interseismic period in the northern region of the Red River fault, where stress builds up in a broad region surrounding the fault.

CRediT authorship contribution statement

Shiming Liang: Data curation, Formal analysis, Writing – original draft. **Rumeng Guo:** Conceptualization, Data curation, Formal analysis, Investigation, Software, Writing – original draft, Project administration, Writing – review & editing. **Hongfeng Yang:** Data curation, Formal analysis, Project administration, Writing – review & editing. **Xiongwei Tang:** Data curation, Writing – original draft. **Xiaoxue Xu:** Data curation, Writing – review & editing. **Weijun Gan:** Data curation, Writing – review & editing.

Declaration of Competing Interest

The authors declare that they have no known competing financial interests or personal relationships that could have appeared to influence the work reported in this paper.

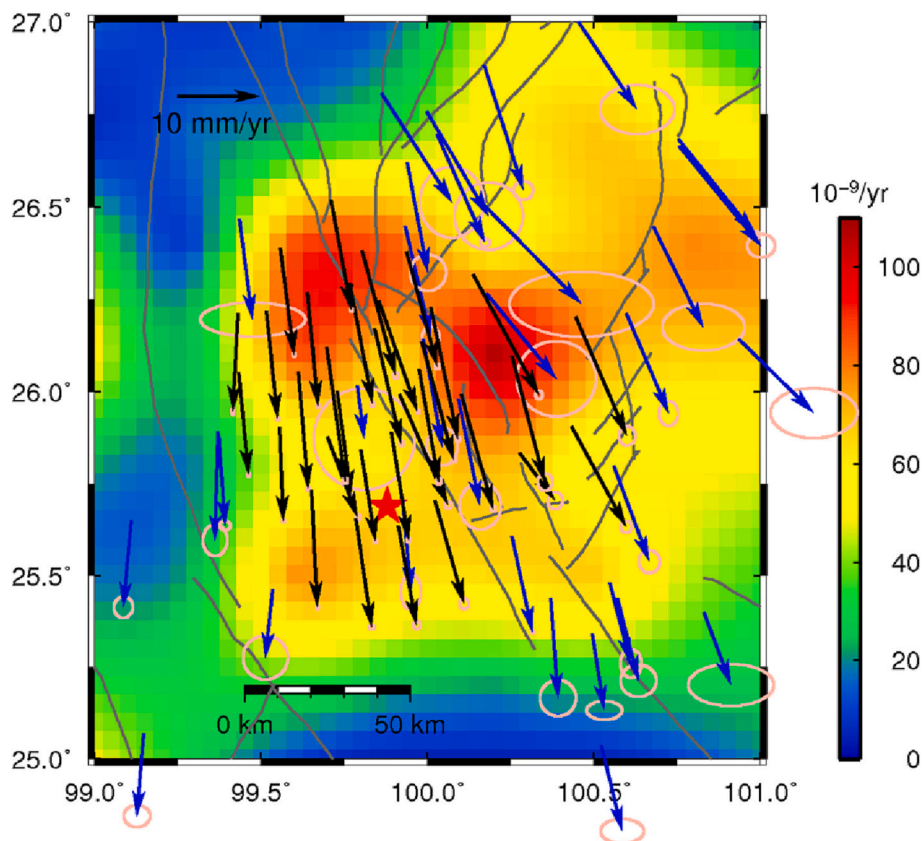


Fig. 12. Strain rates and interseismic GPS velocities. The background represents the second invariant of strain rates. Black and blue arrows denote the interseismic secular velocities from our new-built GPS sites and Wang and Shen (2020), respectively. (For interpretation of the references to colour in this figure legend, the reader is referred to the web version of this article.)

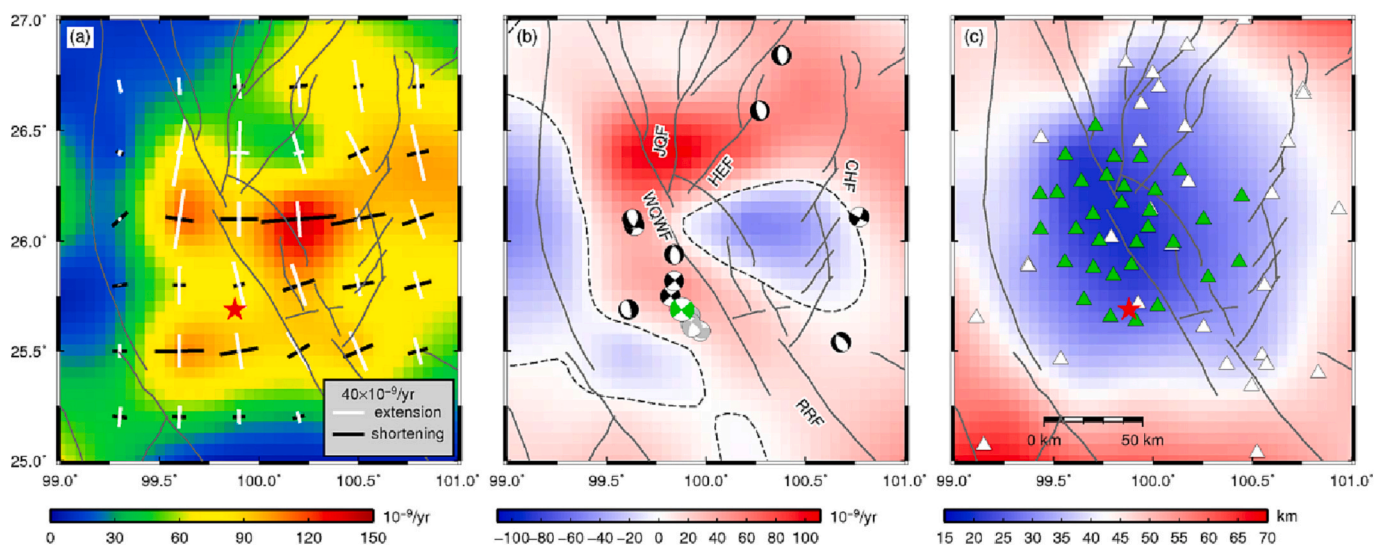


Fig. 13. Interpolated strain rate results using Gaussian and Voronoi cell weighting functions. Distribution of (a) the maximum shear strain rate and (b) the dilatation rate. White and black bars denote the principle strain rates on $0.5^\circ \times 0.5^\circ$ grids. Black and gray beachballs are the focal mechanisms of historical earthquakes from the Global CMT catalog (1976–2020, $M \geq 4.5$) and the Yangbi seismic sequence with $M \geq 4.5$ from Yang et al. (2021b), respectively. The green beachball denotes the focal mechanism of the mainshock from Zhu et al. (2022). Dashed lines represent the dilatation strain rate with zero. (c) The smoothing constant. Green and white triangles denote the new-built and pre-existing GPS stations (from M. Wang & Shen), respectively. The red star denotes the epicenter of the 2021 Yangbi event. HEF: Heqing-Eryuan fault; JQF: Jianchuan-Qiaohou fault. Other symbols are the same as Fig. 1. (For interpretation of the references to colour in this figure legend, the reader is referred to the web version of this article.)

Data availability

The SAR images are obtained from European Space Agency and are

available at <https://scihub.copernicus.eu/>. The data of GPS coordinate time series used in this paper are stored at Harvard Dataverse (<https://doi.org/10.7910/DVN/AH6KHG>). The coseismic and

interseismic GPS observations from our new-built GPS stations are displayed in the supporting information Tables S2 and S3, respectively. The other secular GPS velocities are from the work of M. Wang and Shen (2020), *Journal of Geophysical Research: Solid Earth* (doi:10.1029/2019jb018774). The three-component regional waves are from the China National Digital Seismic Network (<https://doi.org/10.7914/SN/CD>) and the Institute of Engineering Mechanics, China Earthquake Administration (<https://data.earthquake.cn/datashare/report.shtml?PAGEID=datasourcelist&dt=ff80808277cc56050179c55ee7220005>). The focal mechanisms of historical earthquakes are downloaded from the gCMT project (<https://www.globalcmt.org/>).

Acknowledgments

We thank the Editor Ling Chen and three anonymous reviewers for comments that improved our manuscript. This study is supported by the Strategic Priority Research Program of Chinese Academy of Sciences “Formation, evolution and habitability of terrestrial planets” (No. XDB41000000) and the Open Fund of Wuhan, Gravitation and Solid Earth Tides, National Observation and Research Station (No. WHYWZ202111), Hong Kong Research Grants Council (14306122), State Key Lab of Earthquake Dynamics (grant No. LED2021B03).

Appendix A. Supplementary data

Supplementary data to this article can be found online at <https://doi.org/10.1016/j.tecto.2023.229932>.

References

- Bai, D., Unsworth, M.J., Meju, M.A., Ma, X., Teng, J., Kong, X., et al., 2010. Crustal deformation of the eastern Tibetan plateau revealed by magnetotelluric imaging. *Nat. Geosci.* 3 (5), 358–362. <https://doi.org/10.1038/ngeo830>.
- Barbot, S., Fialko, Y., Bock, Y., 2009. Postseismic deformation due to the Mw 6.0 2004 Parkfield earthquake: Stress-driven creep on a fault with spatially variable rate-and-state friction parameters. *J. Geophys. Res. Solid Earth* 114 (B7). <https://doi.org/10.1029/2008JB005748>.
- Barnhart, W.D., Gold, R.D., Hollingsworth, J., 2020. Localized fault-zone dilatancy and surface inelasticity of the 2019 Ridgecrest earthquakes. *Nat. Geosci.* 13 (10), 699–704. <https://doi.org/10.1038/s41561-020-0628-8>.
- Chang, Z., Hao, C., Zang, Y., Dai, B., 2016. Recent active features of Weixi-Qiaohou fault and its relationship with the Honghe fault. *J. Geomech.* 22 (3), 517–530.
- Chen, C.W., Zebker, H.A., 2001. Two-dimensional phase unwrapping with use of statistical models for cost functions in nonlinear optimization. *JOSA A* 18 (2), 338–351. <https://doi.org/10.1364/JOSAA.18.000338>.
- Chen, L., Hao, J., Wang, Z., Xu, T., 2022. The 21 May 2021 Mw 6.1 Yangbi Earthquake—a unilateral rupture event with conjugately distributed aftershocks. *Seismol. Res. Lett.* 93 <https://doi.org/10.1785/0220210241>.
- Cheng, C., Wang, D., Yao, Q., Fang, L., Xu, S., Huang, Z., et al., 2023. The 2021 Mw 7.3 Madoi, China earthquake: transient supershear ruptures on a presumed immature strike-slip fault. *J. Geophys. Res. Solid Earth* 128 (2). <https://doi.org/10.1029/2022JB024641> e2022JB024641.
- Chousianitis, K., Konca, A.O., 2021. Rupture process of the 2020 Mw7.0 Samos earthquake and its effect on surrounding active faults. *Geophys. Res. Lett.* 48 (14) <https://doi.org/10.1029/2021GL094162> e2021GL094162.
- Choy, G.L., Kirby, S.H., 2004. Apparent stress, fault maturity and seismic hazard for normal-fault earthquakes at subduction zones. *Geophys. J. Int.* 159 (3), 991–1012. <https://doi.org/10.1111/j.1365-246X.2004.02449.x>.
- Dolan, J.F., Christofferson, S.A., Shaw, J.H., 2003. Recognition of paleoearthquakes on the Puente Hills blind thrust fault, California. *Science* 300 (5616), 115–118. <https://doi.org/10.1126/science.1080593>.
- Feng, W., Almeida, R.V., 2020. Inelastic earthquake damage. *Nat. Geosci.* 13 (10), 661–662. <https://doi.org/10.1038/s41561-020-0642-x>.
- Fialko, Y., 2004. Evidence of fluid-filled upper crust from observations of postseismic deformation due to the 1992 Mw7.3 Landers earthquake. *J. Geophys. Res. Solid Earth* 109 (B8). <https://doi.org/10.1029/2004JB002985>.
- Fialko, Y., Sandwell, D., Simons, M., Rosen, P., 2005. Three-dimensional deformation caused by the Bam, Iran, earthquake and the origin of shallow slip deficit. *Nature* 435 (7040), 295–299. <https://doi.org/10.1038/nature03425>.
- Freed, A.M., Ali, S.T., Bürgmann, R., 2007. Evolution of stress in Southern California for the past 200 years from coseismic, postseismic and interseismic stress changes. *Geophys. J. Int.* 169 (3), 1164–1179. <https://doi.org/10.1111/j.1365-246X.2007.03391.x>.
- Gallović, F., Zahradník, J., Plicka, V., Sokos, E., Evangelidis, C., Fountoulakis, I., Turhan, F., 2020. Complex rupture dynamics on an immature fault during the 2020 Mw 6.8 Elazığ earthquake, Turkey. *Commun. Earth Environ.* 1 (1), 1–8. <https://doi.org/10.1038/s43247-020-00038-x>.
- Goldberg, D.E., Melgar, D., Sahakian, V.J., Thomas, A.M., Xu, X., Crowell, B.W., Geng, J., 2020. Complex rupture of an immature fault zone: a simultaneous kinematic model of the 2019 Ridgecrest, CA earthquakes. *Geophys. Res. Lett.* 47 (3) <https://doi.org/10.1029/2019GL086382> e2019GL086382.
- Goldstein, R.M., Werner, C.L., 1998. Radar interferogram filtering for geophysical applications. *Geophys. Res. Lett.* 25 (21), 4035–4038. <https://doi.org/10.1029/1998GL900033>.
- Gong, W., Ye, L., Qiu, Y., Lay, T., Kanamori, H., 2022. Rupture Directivity of the 2021 Mw 6.0 Yangbi, Yunnan Earthquake. *J. Geophys. Res. Solid Earth.* <https://doi.org/10.1029/2022JB024321> e2022JB024321.
- Guo, R., Zheng, Y., Tian, W., Xu, J., Zhang, W., 2018. Locking status and earthquake potential Hazard along the Middle-South Xianshuihe Fault. *Remote Sens. (Basel)* 10 (12), 2048. <https://doi.org/10.3390/rs10122048>.
- Guo, R., Zheng, Y., Xu, J., Jiang, Z., 2019. Seismic and aseismic fault slip associated with the 2017 Mw 8.2 Chiapas, Mexico, earthquake sequence. *Seismol. Res. Lett.* 90 (3), 1111–1120. <https://doi.org/10.1785/0220180262>.
- Guo, R., Zheng, Y., An, C., Xu, J., Jiang, Z., Zhang, L., et al., 2020a. The 2018 Mw 7.9 Offshore Kodiak, Alaska, Earthquake: an unusual outer rise strike-slip earthquake. *J. Geophys. Res. Solid Earth* 125 (5). <https://doi.org/10.1029/2019JB019267> e2019JB019267.
- Guo, R., Zheng, Y., Xu, J., 2020b. Stress modulation of the seismic gap between the 2008 Ms 8.0 Wenchuan earthquake and the 2013 Ms 7.0 Lushan earthquake and implications for seismic hazard. *Geophys. J. Int.* 221 (3), 2113–2125. <https://doi.org/10.1093/gji/ggaa143>.
- Guo, R., Yang, H., Li, Y., Zheng, Y., Zhang, L., 2021a. Complex slip distribution of the 2021 Mw 7.4 Maduo, China, earthquake: an event occurring on the slowly slipping fault. *Seismol. Res. Lett.* 93 (2A), 653–665. <https://doi.org/10.1785/0220210226>.
- Guo, R., Yang, H., Zhu, Y., Xu, J., Zhang, L., An, C., 2021b. Narrow rupture of the 020 Mw 7.4 La Crucecita, Mexico, earthquake. *Seismol. Res. Lett.* 92 (3), 1891–1899. <https://doi.org/10.1785/0220200328>.
- Hamiel, Y., Liu, Y., Lyakhovskiy, V., Ben-Zion, Y., Lockner, D., 2004. A viscoelastic damage model with applications to stable and unstable fracturing. *Geophys. J. Int.* 159 (3), 1155–1165. <https://doi.org/10.1111/j.1365-246X.2004.02452.x>.
- Helmlinger, D.V., 1974. Generalized ray theory for shear dislocations. *Bull. Seismol. Soc. Am.* 64 (1), 45–64.
- Heyburn, R., Selby, N.D., Fox, B., 2013. Estimating earthquake source depths by combining surface wave amplitude spectra and teleseismic depth phase observations. *Geophys. J. Int.* 194 (2), 1000–1010. <https://doi.org/10.1093/gji/ggt140>.
- Huang, H., Meng, L., Bürgmann, R., Wang, W., Wang, K., 2020. Spatio-temporal foreshock evolution of the 2019 M 6.4 and M 7.1 Ridgecrest, California earthquakes. *Earth Planet. Sci. Lett.* 551, 116582 <https://doi.org/10.1016/j.epsl.2020.116582>.
- Ji, C., Wald, D.J., Helmlinger, D.V., 2002. Source description of the 1999 Hector Mine, California, earthquake, part I: wavelet domain inversion theory and resolution analysis. *Bull. Seismol. Soc. Am.* 92 (4), 1192–1207. <https://doi.org/10.1785/0120000916>.
- Johnson, K.M., Bürgmann, R., Larson, K., 2006. Frictional properties on the San Andreas Fault near Parkfield, California, inferred from models of afterslip following the 2004 earthquake. *Bull. Seismol. Soc. Am.* 96 (4B), S321–S338. <https://doi.org/10.1785/0120050808>.
- Kaneko, Y., Fialko, Y., 2011. Shallow slip deficit due to large strike-slip earthquakes in dynamic rupture simulations with elasto-plastic off-fault response. *Geophys. J. Int.* 186 (3), 1389–1403. <https://doi.org/10.1111/j.1365-246X.2011.05117.x>.
- Kato, A., Ben-Zion, Y., 2021. The generation of large earthquakes. *Nat. Rev. Earth Environ.* 2 (1), 26–39. <https://doi.org/10.1038/s43017-020-00108-w>.
- Kroll, K.A., Richards-Dinger, K.B., Dieterich, J.H., Cochran, E.S., 2017. Delayed seismicity rate changes controlled by static stress transfer. *J. Geophys. Res. Solid Earth* 122 (10), 7951–7965. <https://doi.org/10.1002/2017JB014227>.
- Kumar, A., Singh, S.K., Mitra, S., Priestley, K.F., Dayal, S., 2017. The 2015 April 25 Gorkha (Nepal) earthquake and its aftershocks: implications for lateral heterogeneity on the Main Himalayan Thrust. *Geophys. J. Int.* 208 (2), 992–1008. <https://doi.org/10.1093/gji/ggw438>.
- Lange, D., Bedford, J.R., Moreno, M., Tilmann, F., Baez, J.C., Bevis, M., Krüger, F., 2014. Comparison of postseismic afterslip models with aftershock seismicity for three subduction-zone earthquakes: Nias 2005, Maule 2010 and Tohoku 2011. *Geophys. J. Int.* 199, 784–799. <https://doi.org/10.1093/gji/ggu292>.
- Lease, R.O., Burbank, D.W., Gehrels, G.E., Wang, Z., Yuan, D., 2007. Signatures of mountain building: Detrital zircon U/Pb ages from northeastern Tibet. *Geology* 35 (3), 239–242. <https://doi.org/10.1130/G23057A.1>.
- Lei, X., Wang, Z., Ma, S., He, C., 2021. A preliminary study on the characteristics and mechanism of the May 2021 Ms6.4 Yangbi earthquake sequence, Yunnan, China. *Acta Seismol. Sin.* 43, 261–286. <https://doi.org/10.11939/jass.20210100>.
- Li, Z., Wang, Y., Gan, W., Fang, L., Zhou, R., Seagren, E.G., et al., 2020. Diffuse deformation in the SE Tibetan Plateau: new insights from geodetic observations. *J. Geophys. Res. Solid Earth* 125 (10). <https://doi.org/10.1029/2020JB019383> e2020JB019383.
- Li, C., Zhang, J., Wang, W., Sun, K., Shan, X., 2021. The seismogenic fault of the 2021 Yunnan Yangbi Ms6.4 earthquake. *Seismol. Geol. (in Chinese)* 43 (3), 706–721. <https://doi.org/10.3969/j.issn.0253-4967.2021.03.015>.
- Li, C., Shan, X., Zhang, G., Zhao, C., Gong, W., Zhang, Y., 2022. Slip kinematics of the 2021 Yangbi earthquake: fore-main-aftershock sequence rupture along an unknown secondary fault of the Weixi–Qiaohou Fault. *Seismol. Res. Lett.* 93 (3), 1400–1412. <https://doi.org/10.1785/0220210220>.
- Liu, C., Zheng, Y., Wang, R., Xiong, X., 2015. Kinematic rupture process of the 2014 Chile Mw 8.1 earthquake constrained by strong-motion, GPS static offsets and teleseismic data. *Geophys. J. Int.* 202 (2), 1137–1145. <https://doi.org/10.1093/gji/ggv214>.

- Liu, C., Lay, T., Pollitz, F.F., Xu, J., Xiong, X., 2021. Seismic and geodetic analysis of rupture characteristics of the 2020 Mw 6.5 Monte Cristo Range, Nevada, earthquake. *Bull. Seismol. Soc. Am.* 111 (6), 3226–3236. <https://doi.org/10.1785/0120200327>.
- Liu, X., Xu, W., He, Z., Fang, L., Chen, Z., 2022. Aseismic slip and cascade triggering process of foreshocks leading to the 2021 Mw 6.1 Yangbi earthquake. *Seismol. Res. Lett.* 93 (3), 1413–1428. <https://doi.org/10.1785/0220210263>.
- Liu, M., Li, H., Zhang, M., Wang, W., Yang, Y., Li, L., et al., 2022a. Investigation of the 2013 Eryuan, Yunnan, China MS 5.5 earthquake sequence: aftershock migration, seismogenic structure and hazard implication. *Tectonophysics* 837, 229445. <https://doi.org/10.1016/j.tecto.2022.229445>.
- Liu, M., Li, H., Li, L., Zhang, M., Wang, W., 2022b. Multistage nucleation of the 2021 Yangbi MS 6.4 earthquake, Yunnan, China and its foreshocks. *J. Geophys. Res. Solid Earth* 127 (5). <https://doi.org/10.1029/2022JB024091>.
- Luo, R., Wu, Z., Xiaolong, H., Zhou, C., Tian, T., 2015. The main active faults and the active tectonic system of Binchuan area, northwestern Yunnan. *Geol. Bull. China* 34, 155–170.
- Lyakhovskiy, V., Ben-Zion, Y., 2009. Evolving geometrical and material properties of fault zones in a damage rheology model. *Geochem. Geophys. Geosyst.* 10 (11) <https://doi.org/10.1029/2009GC002543>.
- Manighetti, I., Campillo, M., Bouley, S., Cotton, F., 2007. Earthquake scaling, fault segmentation, and structural maturity. *Earth Planet. Sci. Lett.* 253 (3), 429–438. <https://doi.org/10.1016/j.epsl.2006.11.004>.
- Manighetti, I., Caulet, C., De Barros, L., Perrin, C., Cappa, F., Gaudemer, Y., 2015. Generic along-strike segmentation of Afar normal faults, East Africa: implications on fault growth and stress heterogeneity on seismogenic fault planes. *Geochem. Geophys. Geosyst.* 16 (2), 443–467. <https://doi.org/10.1002/2014GC005691>.
- Manighetti, I., Mercier, A., De Barros, L., 2021. Fault trace corrugation and segmentation as a measure of fault structural maturity. *Geophys. Res. Lett.* 48 (20) <https://doi.org/10.1029/2021GL095372>.
- Melgar, D., Fan, W., Riquelme, S., Geng, J., Liang, C., Fuentes, M., et al., 2016. Slip segmentation and slow rupture to the trench during the 2015, Mw8.3 Illapel, Chile earthquake. *Geophys. Res. Lett.* 43 (3), 961–966. <https://doi.org/10.1002/2015GL067369>.
- Perfettini, H., Avouac, J.-P., 2007. Modeling afterslip and aftershocks following the 1992 Landers earthquake. *J. Geophys. Res.* Solid Earth 112 (B7). <https://doi.org/10.1029/2006JB004399>.
- Perfettini, H., Frank, W.B., Marsan, D., Bouchon, M., 2018. A model of aftershock migration driven by afterslip. *Geophys. Res. Lett.* 45 (5), 2283–2293. <https://doi.org/10.1002/2017GL076287>.
- Perrin, C., Manighetti, I., Ampuero, J.-P., Cappa, F., Gaudemer, Y., 2016. Location of largest earthquake slip and fast rupture controlled by along-strike change in fault structural maturity due to fault growth. *J. Geophys. Res. Solid Earth* 121 (5), 3666–3685. <https://doi.org/10.1002/2015JB012671>.
- Pollitz, F.F., McCrory, P., Svarc, J., Murray, J., 2008. Dislocation models of interseismic deformation in the western United States. *J. Geophys. Res. Solid Earth* 113 (B4). <https://doi.org/10.1029/2007JB005174>.
- Royden, L.H., Burchfiel, B.C., van der Hilst, R.D., 2008. The geological evolution of the Tibetan Plateau. *Science* 321 (5892), 1054–1058. <https://doi.org/10.1126/science.1155371>.
- Sadeghi Chorsi, T., Braunmiller, J., Deng, F., Dixon, T.H., 2022. Afterslip from the 2020 M 6.5 Monte Cristo Range, Nevada earthquake. *Geophys. Res. Lett.* 49 (17) <https://doi.org/10.1029/2022GL099952>.
- Sandwell, D., Mellors, R., Tong, X., Wei, M., Wessel, P., 2011. Open radar interferometry software for mapping surface deformation. *Eos, Trans. Am. Geophys. Union* 92 (28), 234. <https://doi.org/10.1029/2011EO280002>.
- Shen, Z.-K., Lü, J., Wang, M., Bürgmann, R., 2005. Contemporary crustal deformation around the southeast borderland of the Tibetan Plateau. *J. Geophys. Res. Solid Earth* 110 (B11). <https://doi.org/10.1029/2004JB003421>.
- Shen, Z.-K., Jackson, D.D., Kagan, Y.Y., 2007. Implications of geodetic strain rate for future earthquakes, with a five-year forecast of M5 earthquakes in southern California. *Seismol. Res. Lett.* 78 (1), 116–120. <https://doi.org/10.1785/gssrl.78.1.116>.
- Shen, Z., Wang, M., Zeng, Y., Wang, F., 2015. Optimal interpolation of spatially discretized geodetic data. *Bull. Seismol. Soc. Am.* 105 (4), 2117–2127. <https://doi.org/10.1785/0120140247>.
- Shi, X., Sieh, K., Weldon, R., Zhu, C., Han, Y., Yang, J., Robinson, S.W., 2018. Slip rate and rare large prehistoric earthquakes of the Red River Fault, southwestern China. *Geochem. Geophys. Geosyst.* 19 (7), 2014–2031. <https://doi.org/10.1029/2017GC007420>.
- Simpson, R.W., Reasenber, P., 1994. Earthquake-induced static-stress changes on Central California faults. In: U.S. Geological Survey Professional Paper 1550, pp. F55–F89.
- Su, J., Liu, M., Zhang, Y., Wang, W., Li, H., Yang, J., et al., 2021. High resolution earthquake catalog building for the 21 May 2021 Yangbi, Yunnan, Ms6.4 earthquake sequence using deep-learning phase picker. *Chin. J. Geophys. (in Chinese)* 64 (8), 2647–2656.
- Sun, Q., Guo, Z., Pei, S., Fu, Y.V., Chen, Y.J., 2022. Fluids triggered the 2021 Mw 6.1 Yangbi earthquake at an unmapped fault: implications for the tectonics at the northern end of the Red River Fault. *Seismol. Res. Lett.* 93 (2A), 666–679. <https://doi.org/10.1785/0220210227>.
- Thakur, P., Huang, Y., 2021. Influence of fault zone maturity on fully dynamic earthquake cycles. *Geophys. Res. Lett.* 48 (17) <https://doi.org/10.1029/2021GL094679>.
- Wang, M., Shen, Z.-K., 2020. Present-day crustal deformation of continental China derived from GPS and its tectonic implications. *J. Geophys. Res. Solid Earth* 125 (2). <https://doi.org/10.1029/2019JB018774>.
- Wang, T., Wei, S., Shi, X., Qiu, Q., Li, L., Peng, D., et al., 2018. The 2016 Kaikōura earthquake: simultaneous rupture of the subduction interface and overlying faults. *Earth Planet. Sci. Lett.* 482, 44–51. <https://doi.org/10.1016/j.epsl.2017.10.056>.
- Wang, Y., Chen, K., Shi, Y., Zhang, X., Chen, S., Li, P., Lu, D., 2021. Source model and simulated strong ground motion of the 2021 Yangbi, China shallow earthquake constrained by InSAR observations. *Remote Sens. (Basel)* 13 (20), 4138. <https://doi.org/10.3390/rs13204138>.
- Wang, W., He, J., Wang, X., Zhou, Y., Hao, J., Zhao, L., Yao, Z., 2022. Rupture process models of the Yangbi and Maduo earthquakes that struck the eastern Tibetan Plateau in May 2021. *Sci. Bull.* 67 (5), 466–469. <https://doi.org/10.1016/j.scib.2021.11.009>.
- Wei, M., Sandwell, D., Fialko, Y., 2009. A silent Mw 4.7 slip event of October 2006 on the Superstition Hills fault, southern California. *J. Geophys. Res. Solid Earth* 114 (B7). <https://doi.org/10.1029/2008JB006135>.
- Wen, X., Ma, S., Fang, L., Liang, M., Du, F., Long, F., Zhao, X., 2022. Complex structural fault system and distributed deformation across the Big Bend of the Red River fault, Yunnan, China. *Phys. Earth Planet. In.* 106942 <https://doi.org/10.1016/j.pepi.2022.106942>.
- Wesnousky, S.G., 1988. Seismological and structural evolution of strike-slip faults. *Nature* 335 (6188), 340–343. <https://doi.org/10.1038/335340a0>.
- Xie, X., Yao, Z., 1989. A generalized reflection-transmission coefficient matrix method to calculate static displacement field of a dislocation source in a stratified half space. *Chin. J. Geophys.* 32, 191–205.
- Xie, Z., Jin, B., Zheng, Y., Ge, C., Xiong, X., Xiong, C., Hsu, H., 2013. Source parameters inversion of the 2013 Lushan earthquake by combining teleseismic waveforms and local seismograms. *Sci. China Earth Sci.* 56 (7), 1177–1186. <https://doi.org/10.1007/s11430-013-4640-3>.
- Xu, X., Ji, L., Zhu, L., Wang, G., Zhang, W., Li, N., 2021. The coseismic deformation characteristics and seismogenic structure of the Yangbi Ms6.4 earthquake. *Seismol. Geol. (in Chinese)* 43 (4), 771–789.
- Yan, K., Wang, W., Peng, F., Wang, Q., Kou, H., Yuan, A., 2022. The seismogenic structures and migration characteristics of the 2021 Yangbi Ms6.4 Earthquake sequence in Yunnan, China. *Sci. China Earth Sci.* 65 (8), 1522–1537. <https://doi.org/10.1007/s11430-021-9933-1>.
- Yang, H., Yao, S., 2021. Shallow destructive earthquakes. *Earthquake Sci.* 34 (1), 15–23. <https://doi.org/10.29382/eqs-2020-0072>.
- Yang, H., Moresi, L.N., Quigley, M., 2020. Fault spacing in continental strike-slip shear zones. *Earth Planet. Sci. Lett.* 530, 115906 <https://doi.org/10.1016/j.epsl.2019.115906>.
- Yang, T., Li, B., Fang, L., Su, Y., Zhong, Y., Yang, J., et al., 2021a. Relocation of the foreshocks and aftershocks of the 2021 Ms6.4 Yangbi earthquake sequence, Yunnan, China. *J. Earth Sci.* <https://doi.org/10.1007/s12583-021-1527-7>.
- Yang, Z., Liu, J., Zhang, X.-M., Deng, W., Du, G., Wu, X., 2021b. A preliminary report of the Yangbi, Yunnan, Ms6.4 earthquake of May 21, 2021. *Earth Planet. Phys.* 5 (4), 362–364. <https://doi.org/10.26464/epp2021036>.
- Yu, C., Li, Z., Penna, N.T., Crippa, P., 2018. Generic atmospheric correction model for interferometric synthetic aperture radar observations. *J. Geophys. Res. Solid Earth* 123 (10), 9202–9222. <https://doi.org/10.1029/2017JB015305>.
- Yue, H., Lay, T., Rivera, L., An, C., Vigny, C., Tong, X., Báez Soto, J.C., 2014. Localized fault slip to the trench in the 2010 Maule, Chile Mw = 8.8 earthquake from joint inversion of high-rate GPS, teleseismic body waves, InSAR, campaign GPS, and tsunami observations. *J. Geophys. Res. Solid Earth* 119 (10), 7786–7804. <https://doi.org/10.1002/2014JB011340>.
- Yue, H., Ross, Z.E., Liang, C., Michel, S., Fattahi, H., Fielding, E., et al., 2017. The 2016 Kumamoto Mw = 7.0 earthquake: a significant event in a fault–volcano system. *J. Geophys. Res. Solid Earth* 122 (11), 9166–9183. <https://doi.org/10.1002/2017JB014525>.
- Zeng, Y., Petersen, M.D., Shen, Z.-K., 2018. Earthquake potential in California–Nevada implied by correlation of strain rate and seismicity. *Geophys. Res. Lett.* 45 (4), 1778–1785. <https://doi.org/10.1002/2017GL075967>.
- Zhang, P.-Z., 2013. Beware of slowly slipping faults. *Nat. Geosci.* 6 (5), 323–324. <https://doi.org/10.1038/ngeo1811>.
- Zhang, K., Gan, W., Liang, S., Xiao, G., Dai, C., Wang, Y., et al., 2021a. Coseismic displacement and slip distribution of the 2021 May 21, Ms6.4, Yangbi earthquake from GNSS observations. *Chin. J. Geophys. (in Chinese)* 64 (7), 2253–2266. <https://doi.org/10.6038/cjg202100524>.
- Zhang, Y., An, Y., Long, F., Zhu, G., Qin, M., Zhong, Y., et al., 2021b. Short-term foreshock and aftershock patterns of the 2021 Ms 6.4 Yangbi earthquake sequence. *Seismol. Res. Lett.* 93 (1), 21–32. <https://doi.org/10.1785/0220210154>.
- Zheng, G., Wang, H., Wright, T.J., Lou, Y., Zhang, R., Zhang, W., et al., 2017. Crustal deformation in the India–Eurasia collision zone from 25 years of GPS measurements. *J. Geophys. Res. Solid Earth* 122 (11), 9290–9312. <https://doi.org/10.1002/2017JB014465>.
- Zhou, Y., Ghosh, A., Fang, L., Yue, H., Zhou, S., Su, Y., 2021. A high-resolution seismic catalog for the 2021 MS6.4/MW6.1 Yangbi earthquake sequence, Yunnan, China: application of AI picker and matched filter. *Earthquake Sci.* 34 (5), 390–398. <https://doi.org/10.29382/eqs-2021-0031>.
- Zhou, Y., Ren, C., Ghosh, A., Meng, H., Fang, L., Yue, H., et al., 2022. Seismological characterization of the 2021 Yangbi foreshock-mainshock sequence, Yunnan, China:

- more than a triggered cascade. *J. Geophys. Res. Solid Earth*. <https://doi.org/10.1029/2022JB024534> e2022JB024534.
- Zhu, L., Rivera, L.A., 2002. A note on the dynamic and static displacements from a point source in multilayered media. *Geophys. J. Int.* 148 (3), 619–627. <https://doi.org/10.1046/j.1365-246X.2002.01610.x>.
- Zhu, G., Yang, H., Tan, Y.J., Jin, M., Li, X., Yang, W., 2022. The cascading foreshock sequence of the Ms 6.4 Yangbi earthquake in Yunnan, China. *Earth Planet. Sci. Lett.* 591, 117594 <https://doi.org/10.1016/j.epsl.2022.117594>.